GDCh Forschungsartikel Angewandte Chemie www.angewandte.org

Zitierweise: Angew. Chem. Int. Ed. **2024**, e202410971
doi.org/10.1002/anie.202410971

Aqueous Proton Batteries

Proton Intercalation into an Open-Tunnel Bronze Phase with Near-Zero Volume Change

*Kosuke Kawai, Seong-Hoon Jang, Yuta Igarashi, Koji Yazawa, Kazuma Gotoh, Jun Kikkawa, Atsuo Yamada, Yoshitaka Tateyama, and Masashi Okubo**

Abstract: Managing safety and supply-chain risks associated with lithium-ion batteries (LIBs) is an urgent task for sustainable development. Aqueous proton batteries are attractive alternatives to LIBs because using water and protons addresses these two risks. However, most host materials undergo large volume changes upon H^+ intercalation, which induces intraparticle cracking to accelerates parasitic reactions. Herein, we report that $Mo_3Nb_2O_{14}$ bronze exhibits reversible H^+ intercalation (200 mAh g^{-1}) with a Coulombic efficiency of 99.7 % owing to near-zero volume change and solid-solution-type phase transition. Combination of experimental and theoretical analyses clarifies that rotation and shrinkage of open tunnels, which consist of flexible corner-sharing Mo/NbO$_n$ polyhedra, relieve local structural distortions upon H^+ intercalation to suppress intraparticle cracking. The prototype full cell of an aqueous proton battery with a $Mo_3Nb_2O_{14}$ anode operates stably over 1000 charge/discharge cycles. This study reveals the importance of implementing distortion-relieving voids in host materials to reduce volume change upon charge/discharge.

Introduction

Electrochemical energy storage (EES) is vital for building a sustainable society because supplying intermittent power from renewables to an electrical grid must be load-leveled using EES systems. Currently, lithium-ion batteries (LIBs) dominate the EES market owing to their high energy densities, high energy efficiencies, and long cycle lives.[1] However, flammable organic electrolytes pose intrinsic risks of fire and explosion accidents. Therefore, replacing flammable organic electrolytes with non-flammable aqueous electrolytes is highly desirable. Furthermore, the global maldistribution of lithium resources provides severe supply-chain risks that impede the mass production of large EES systems. Aqueous proton batteries are regarded as promising alternatives to LIBs for managing safety and supply-chain risks. Proton is the cation with the smallest ionic radius,[2] which enables host materials to be densely protonated with minimal lattice distortion during charging.

Stable operation of an aqueous proton battery requires suppressing parasitic side reactions (e.g., the hydrogen-evolution reactions (HER), oxygen-evolution reactions (OER), and electrode-material dissolution), which are induced mainly by high water-molecule activity. Aqueous electrolytes with less water-molecule activities have been developed extensively. "Water-in-salt" electrolytes reduce water-molecule activity by forming coordination bonds between water molecules and excess cations.[3] Water molecules in "water-in-sugar" electrolytes form hydrogen

---

[*] K. Kawai, Y. Igarashi, M. Okubo
Department of Electrical Engineering and Bioscience, School of Advanced Science and Engineering, Waseda University, 3-4-1 Okubo, Shinjuku-ku, Tokyo 169-8555, Japan
E-mail: m-okubo@waseda.jp

S.-H. Jang, Y. Tateyama
Research Center for Energy and Environmental Materials (GREEN), National Institute for Materials Science (NIMS), 1-1 Namiki, Tsukuba, Ibaraki 305-0044, Japan

S.-H. Jang
Institute for Materials Research, Tohoku University, 2-1-1 Katahira, Aoba-ku, Sendai, Miyagi 980-8577, Japan

K. Yazawa
JEOL Ltd., 3-1-2 Musashino, Akishima, Tokyo 196-8558, Japan

K. Gotoh
Center for Nano Materials and Technology (CNMT), Japan Advanced Institute of Science and Technology (JAIST), 1-1 Asahidai, Nomi, Ishikawa, 923-1292, Japan

J. Kikkawa
Center for Basic Research on Materials (CBRM), National Institute for Materials Science (NIMS), 1-1 Namiki, Tsukuba, Ibaraki 305-0044, Japan

A. Yamada
Department of Chemical System Engineering, School of Engineering, The University of Tokyo, 7-3-1 Hongo, Bunkyo-ku, Tokyo 113-8656, Japan

A. Yamada
Sungkyunkwan University Institute of Energy Science & Technology (SIEST), Sungkyunkwan University, Suwon 16419, Korea

Y. Tateyama
Tokyo Institute of Technology (Tokyo Tech), 4259 Nagatsuta-cho, Midori-ku, Yokohama, 226-8501, Japan

M. Okubo
Kagami Memorial Research Institute for Material Science and Technology, Waseda University, Tokyo 169-0051, Japan

bonds with sugar additives, which significantly decreases water-molecule activity.[4] Another option involves the "molecular crowding" effect: molecular crowding agents such as polyethylene glycol (PEG) form hydrogen bonds with water molecules to reduce water-molecule activity.[5] As a consequence, parasitic reactions are significantly suppressed at the electrode-electrolyte interface.

Active materials should be highly durable against mechanical stress and chemical changes upon charge/discharge to further suppress electrode performance degradation. In particular, volume expansion/shrinkage can crack active materials, with the newly exposed surfaces accelerating interfacial parasitic reactions. For example, layered α-MoO_3 exhibits monoclinic distortion and undergoes a volume change ($\Delta V/V = 5.5\,\%$) upon H^+ intercalation, resulting in severe intraparticle cracking.[6] Other hosts materials (V_2O_3 and h-$WO_3 \cdot 0.6H_2O$) also suffer from volume changes upon H^+ intercalation, resulting in performance degradation.[7] The microscopic origins of these structural transformation involve either expansion/contraction of the interlayer distance between loosely stacked layers or the local distortion of MO_n polyhedra upon H^+ intercalation. H^+ intercalation with near-zero volume change, which is required for stable operation of an aqueous proton battery, has rarely been reported.

In this study, we report $Mo_3Nb_2O_{14}$ as a H^+-intercalation host structure for aqueous rechargeable batteries (Figure 1a). $Mo_3Nb_2O_{14}$ is categorized as a bronze phase with a general MO_{3-x} (M = Mo, Nb, W) formula. Edge- and corner-sharing Mo/NbO_n (n = 6 and 7) polyhedra form the flexible framework with open tunnels that undergo rotation and shrinkage to relieve local structural distortion upon H^+ intercalation. Consequently, $Mo_3Nb_2O_{14}$ exhibits a Coulombic efficiency of 99.7 % without intraparticle cracking owing to near-zero volume change as well as solid-solution-type phase transition upon H^+ intercalation.

Results and Discussion

$Mo_3Nb_2O_{14}$ was synthesized using a conventional solid-state synthesis method. The synchrotron powder X-ray diffraction (XRD) pattern of the synthesized sample is refined with $P4/mbm$ space group. The refined lattice constants, namely $a = 23.161(5)$ Å and $c = 3.9984(8)$ Å, are in good agreement with those reported previously (Figure S1).[8] Scanning electron microscopy shows an irregular block-like morphology owing to preferential growth along the c-axis, which is typical of open-tunnel bronze phases (Figure S2). Elemental maps acquired by energy-dispersive X-ray spectroscopy reveal

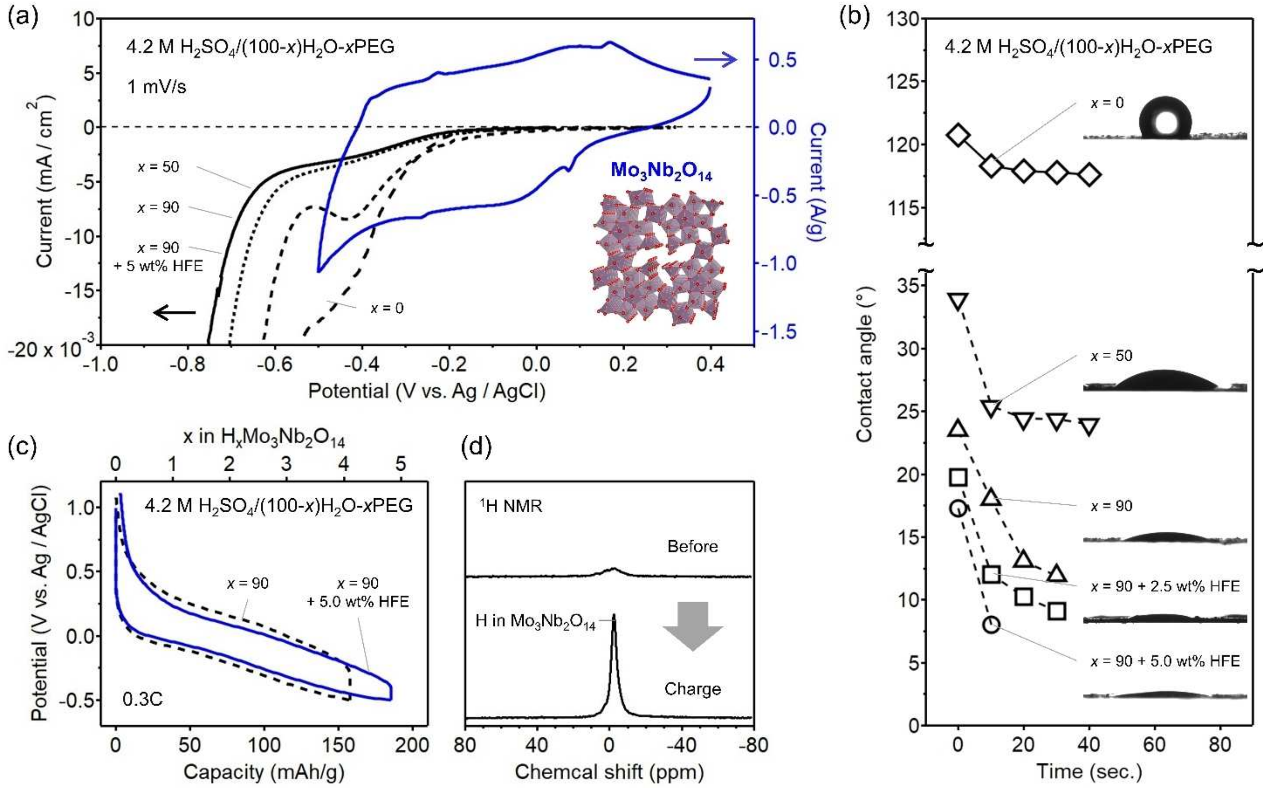

Figure 1. Proton intercalation into $Mo_3Nb_2O_{14}$ in molecular crowding electrolytes. (a) LSV curves of electrolytes on Ti foil (black) and CV curves of $Mo_3Nb_2O_{14}$ (blue) acquired at 1 mV s^{-1}. The inset shows the crystal structure of $Mo_3Nb_2O_{14}$. (b) Contact angles as functions of time after dropping electrolytes onto $Mo_3Nb_2O_{14}$ electrodes. The insets show optical images of electrolyte droplets on $Mo_3Nb_2O_{14}$ electrodes; they were recorded 10 s after dropping each electrolyte. (c) Galvanostatic charge/discharge curves at a specific current of 58 mA g^{-1} (0.3 C) with a cutoff potential between −0.5 and 1.1 V vs. Ag/AgCl. (d) 1H MAS NMR spectra of $H_xMo_3Nb_2O_{14}$ before and after charging to −0.5 V vs. Ag/AgCl.

uniformly distributed Mo and Nb with a Mo/Nb atomic ratio of 1.5 (Figure S3). These results confirm the successful synthesis of $Mo_3Nb_2O_{14}$ bronze.

Sulfuric-acid-based electrolytes were used for H^+ intercalation into $Mo_3Nb_2O_{14}$ electrodes. Sulfuric acid was diluted to 4.2 mol$\,L^{-1}$ in a "molecular crowding" aqueous solution of $(100-x)H_2O-x$PEG ($x=0$, 50, and 90), after which 2.5 or 5.0 wt% 1,1,2,2-tetrafluoroethyl 2,2,3,3-tetrafluoropropyl ether (HFE) was added to improve electrolyte wettability on the $Mo_3Nb_2O_{14}$ electrode. Flammability testing shows that the resulting electrolytes do not ignite, confirming their high safety (Figure S4). Linear sweep voltammetry (LSV) at 1 mV$\,s^{-1}$ using a Ti current collector shows that 4.2 mol$\,L^{-1}$ $H_2SO_4/100H_2O$ ($x=0$) exhibits cathodic current flow at −0.2 V vs. Ag/AgCl due to the HER (Figure 1a). Although slight reduction current, which may originate from decomposition of specifically adsorbed water molecules on a Ti current collector, is observed at −0.2 V (vs Ag/AgCl) for each electrolyte, increasing the PEG content reduces HER-current flow owing to the molecular crowding effect (i.e., a reduction in water activity by the formation of hydrogen bonds between H_2O and PEG). It should also be noted that anodic stability is improved by increasing the PEG content because anodic corrosion of the current collector and the OER are suppressed by reduced activities of H_2O/H_3O^+ in molecular crowding electrolytes (Figure S5).[9] Consequently, an electrolyte comprising 4.2 mol$\,L^{-1}$ $H_2SO_4/10H_2O-90$PEG ($x=90$) successfully provides a stable cyclic voltammogram for the $Mo_3Nb_2O_{14}$ electrode over a wide potential range (−0.45 to 0.4 V vs. Ag/AgCl). Dynamic contact-angle measurement (Figure 1b) shows a contact angle of 118° for 4.2 mol$\,L^{-1}$ $H_2SO_4/100H_2O$ ($x=0$), which implies highly hydrophobic electrode-electrolyte interface. This hydrophobicity is improved by adding PEG (lower contact angles of 24° and 12° are recorded at $x=50$ and 90, respectively). Furthermore, adding HFE improves the wettability of the PEG-based electrolyte on the $Mo_3Nb_2O_{14}$ electrode; hence static contact angles are unable to be measured owing to the complete permeation of electrolyte droplets into the pores of the electrode. For 4.2 mol$\,L^{-1}$ $H_2SO_4/10H_2O-90PEG+y$ wt% HFE, rates of droplet expansion during the first ten seconds are −0.55, −0.77, and −0.92 °/s for $y=0$, 2.5, and 5.0, respectively, indicating improved wettability of the electrolytes by adding HFE diluent. Presumably, PEG and HFE are preferentially adsorb on the electrode surface to reduce activities of H_2O/H_3O^+ at the solid-electrolyte interface, leading to the suppression of parasitic reactions such as the HER and OER.[5b]

Galvanostatic charge/discharge of the $Mo_3Nb_2O_{14}$ electrode with the 4.2 mol$\,L^{-1}$ $H_2SO_4/10H_2O-90$PEG ($x=90$) electrolyte (Figure 1c) affords a specific capacity of 158 mAh$\,g^{-1}$ at a specific current of 58 mA$\,g^{-1}$ (0.3 C) during the second discharge. Here, "charge" and "discharge" refer to the cathodic (H^+ intercalation) and anodic (H^+ deintercalation) processes, respectively. Meanwhile, an HFE-added electrolyte (4.2 mol$\,L^{-1}$ $H_2SO_4/10H_2O-90$PEG ($x=90$) + 5 wt% HFE) largely reduces polarization during charge/discharge to deliver a larger specific capacity of 185 mAh$\,g^{-1}$, which is comparable to that observed for Li^+ (de)intercalation using a non-aqueous electrolyte (Figure S6).

Ex situ analyses were used to clarify the origin of the stable H^+ (de)intercalation in $Mo_3Nb_2O_{14}$. The ^{1}H solid-state magic-angle-spinning nuclear magnetic resonance (MAS NMR) demonstrates that a sharp peak emerges at a chemical shift of −2.5 ppm, which originates from bare H^+ in oxide compounds, confirming H^+ intercalation into $Mo_3Nb_2O_{14}$ after charge (Figure 1d). Note that H_3O^+ exhibits a chemical shift of 12 ppm in a solid.[10] The Mo *K*-edge X-ray absorption near edge structure (XANES) spectrum of pristine $Mo_3Nb_2O_{14}$ is almost identical to that of MoO_3; hence, the oxidation state of Mo in pristine $Mo_3Nb_2O_{14}$ is +6 (Figure S7). The Mo *K*-edge XANES spectrum shifts reversibly upon charge/discharge, indicating reversible $Mo^{6+}/Mo^{5+}/Mo^{4+}$ redox reactions. The Nb *K*-edge XANES spectrum of pristine $Mo_3Nb_2O_{14}$ is identical to that of Nb_2O_5 (Nb^{5+}); it shifts slightly and reversibly upon charge/discharge, albeit with a much higher absorption energy than that observed for NbO_2 (Nb^{4+}). Although X-ray photoelectron spectroscopy reveals the presence of Nb^{4+} at the surface (Figure S8), the main charge-compensation mechanism for H^+ intercalation in $Mo_3Nb_2O_{14}$ involves the $Mo^{6+}/Mo^{5+}/Mo^{4+}$ redox reactions, with the minor Nb^{5+}/Nb^{4+} contribution.

Figure 2a displays charge/discharge curves at a specific current of 58 mA$\,g^{-1}$ (0.3 C) using the optimal electrolyte (4.2 mol$\,L^{-1}$ $H_2SO_4/10H_2O-90$PEG ($x=90$) + 5 wt% HFE). The specific capacity increases slightly with repeated charge/discharge cycling in the early stage, presumably due to the formation of a superior electrode-electrolyte interface, and finally reaches 200 mAh$\,g^{-1}$ with a Coulombic efficiency of 99.7% at the 40th cycle. Irreversible capacity is recovered during the first cycle when a constant-current constant-voltage mode is applied (Figure S9), which implies sluggish H^+ diffusion or the electronically insulating nature of $Mo_3Nb_2O_{14}$ at the end of the discharge process. Indeed, the galvanostatic intermittent titration technique reveals that polarization of $H_{0.5}Mo_3Nb_2O_{14}$ is ten-fold greater than that of $H_{4.5}Mo_3Nb_2O_{14}$ (Figure S10). Transmission electron microscopy images show a coherent lattice fringe and no intraparticle cracking over the entire surface of a $Mo_3Nb_2O_{14}$ particle, indicative of a highly stable electrode-electrolyte interface (Figure S11). At a specific capacity of 192 mA$\,g^{-1}$ (1 C), the $Mo_3Nb_2O_{14}$ electrode delivers an average Coulombic efficiency of 99.99% over 500 cycles (Figure 2b). Note that other H^+-intercalation host materials, including α-MoO_3, show lower Coulombic efficiency (~99%) in aqueous electrolytes (Table S1).

The specific capacity of the $Mo_3Nb_2O_{14}$ electrode decreases from 185 to 21 mAh$\,g^{-1}$ as a C-rate increases from 0.3 to 30 C rate, with a cutoff potential between −0.5 and 1.1 V vs. Ag/AgCl in 4.2 mol$\,L^{-1}$ $H_2SO_4/10H_2O-90$PEG ($x=90$) + 5 wt% HFE (Figure 2c). Note that the 4.2 mol$\,L^{-1}$ $H_2SO_4/50H_2O-50$PEG ($x=50$) electrolyte, which possesses higher ionic conductivity (126 mS$\,cm^{-1}$) than its $10H_2O-90$PEG ($x=90$) + 5 wt% HFE counterpart (2.2 mS$\,cm^{-1}$), provides a superior rate capability, with a

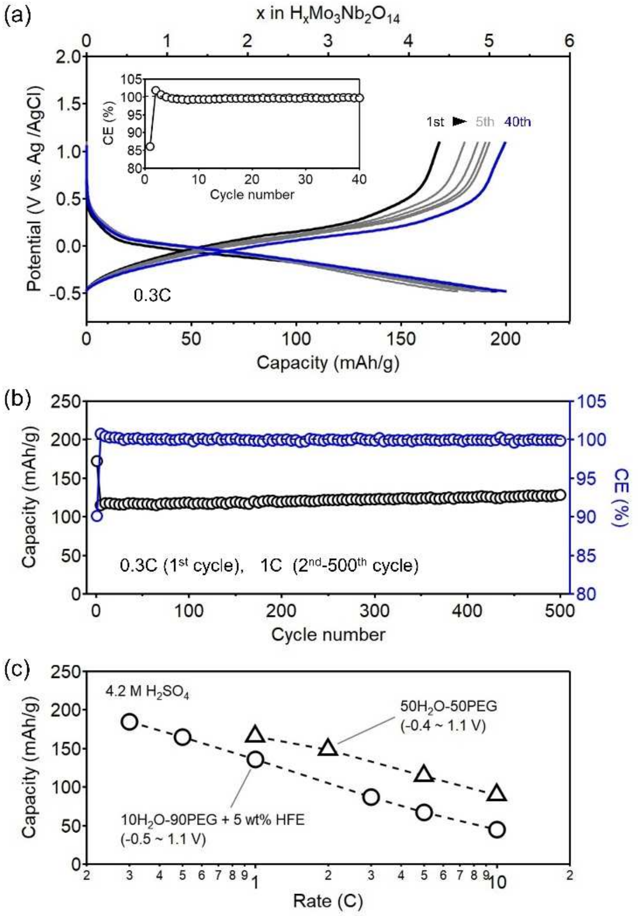

Figure 2. Charge/discharge performance of $Mo_3Nb_2O_{14}$ electrodes in 4.2 mol L^{-1} H_2SO_4/10H$_2$O−90PEG + 5 wt% HFE. (a) Galvanostatic charge/discharge curves at a specific current of 58 mA g^{-1} (0.3 C). (b) Cycle performance at a specific current of 192 mA g^{-1} (1 C). The cutoff voltage is between −0.5 and 1.1 V vs. Ag/AgCl. A low current density of 58 mA g^{-1} (0.3 C) was applied for the first cycle to activate electrode performance. (c) Rate performance of $Mo_3Nb_2O_{14}$ electrodes in 4.2 mol L^{-1} H_2SO_4/10H$_2$O−90PEG + 5 wt% HFE with a cutoff voltage between −0.5 and 1.1 V vs. Ag/AgCl, and 4.2 mol L^{-1} H_2SO_4/50H$_2$O−50PEG with a cutoff voltage between −0.4 and 1.1 V vs. Ag/AgCl.

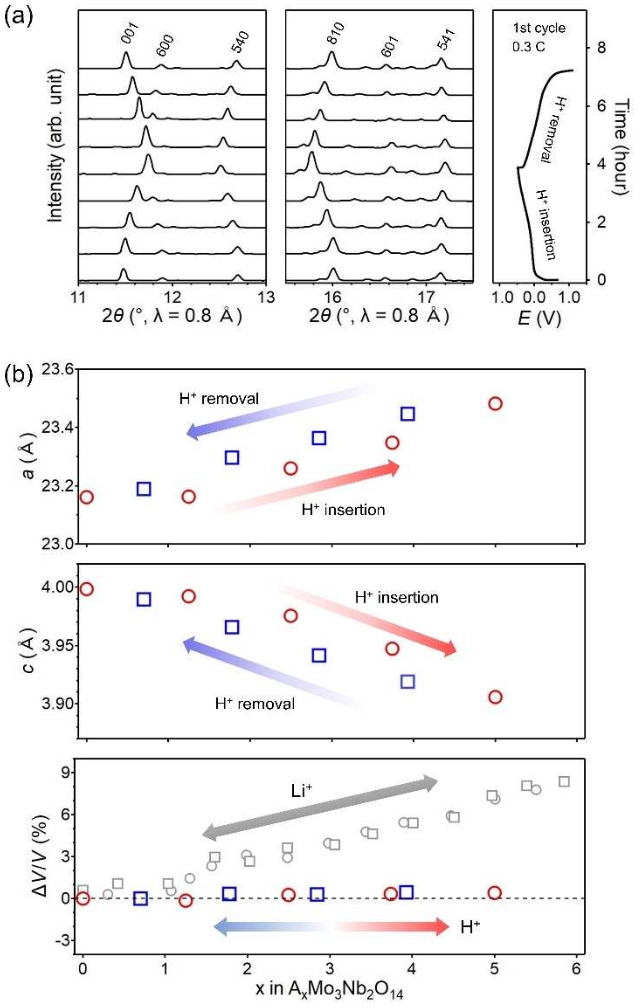

Figure 3. Strain-free H$^+$ intercalation of $Mo_3Nb_2O_{14}$. (a) Ex situ powder XRD patterns of $H_xMo_3Nb_2O_{14}$. (b) Lattice-parameter and lattice-volume transitions for $A_xMo_3Nb_2O_{14}$ (A = H, red and blue symbols; A = Li, gray symbols). The data for $Li_xMo_3Nb_2O_{14}$ are taken from Luo et al.[11]

cutoff potential between −0.4 and 1.1 V vs. Ag/AgCl (Figure S12). Hence, H$^+$ transport in the electrolyte is the rate-determining step rather than H$^+$ diffusion in $Mo_3Nb_2O_{14}$.

Synchrotron powder XRD patterns of the $Mo_3Nb_2O_{14}$ electrodes were recorded during the first cycle (Figure 3a). All the Bragg peaks are indexed using the single-phase model with the *P*4/*mbm* space group for each state-of-charge (Figure S13). The *hk*0 peaks shifts to lower 2θ while the 00 *l* peaks shift to higher 2θ upon H$^+$ intercalation, which indicates the solid-solution-type phase transition with expansion of the *ab*-plane and shrinkage of the *c*-axis upon H$^+$ intercalation. All the Bragg peaks return to their original 2θ positions upon H$^+$ deintercalation, confirming the reversible structural transformation. Figure 3b shows lattice parameters as a function of x in $H_xMo_3Nb_2O_{14}$. Five-H$^+$ intercalation per formula unit leads to small changes in the values of the *a* and *c* lattice parameters (by +1.4 % and −2.3 %, respectively). Importantly, an accumulated change in the unit-cell volume ($\Delta V/V$) is only +0.4 % even after the full charge. The near-zero volume change as well as the solid-solution-type phase transition minimize lattice strain in the $Mo_3Nb_2O_{14}$. Indeed, no apparent cracks are observed in the $Mo_3Nb_2O_{14}$ particles after H$^+$ intercalation (Figure S11). It should be emphasized that Li$^+$ intercalation in $Mo_3Nb_2O_{14}$ results in a large volume change (~8 %),[11] and the cathodic peak at 2.5 V vs. Li/Li$^+$ in its dQ/dV plot fades rapidly with charge/discharge cycling (Figure S14). In contrast, all dQ/dV peaks for H$^+$ (de)intercalation are retained even after 40 cycles. The near-zero volume change of $Mo_3Nb_2O_{14}$ upon H$^+$ intercalation is most likely attained by (i) the smaller ionic radius of H$^+$ (8.3×10^{-6} Å) compared to that of Li$^+$ (0.76 Å), (ii) the dense oxide-ion arrays of the bronze phase, which is favorable for H$^+$ conduction, and (iii) open tunnels that relieve any local distortion induced by H$^+$ intercalation.

The local structural changes in $Mo_3Nb_2O_{14}$ upon H^+ intercalation were analyzed using Rietveld refinement for the ex situ XRD patterns (Figure S15). After H^+ intercalation, the open tunnel in $Mo_3Nb_2O_{14}$ shrinks by 4.4 % (Figure 4a) and rotates 3.9° around the *c*-axis (Figure 4b) owing to the flexible corner-sharing Mo/NbO_n polyhedra. These two local structural changes relieve expansion of the *ab*-plane upon H^+ intercalation. Meanwhile, transition-metal sites, which originally split along the *c*-axis owing to the second Jahn-Teller distortion of Mo/Nb,[12] merge at the center of *c*-axis ($z=0.5$) upon H^+ intercalation (Figure S16). Consequently, the shrinkage of *c*-axis compensates for the expansion of *a*-axis, resulting in the near-zero volume change upon H^+ intercalation in $Mo_3Nb_2O_{14}$. This microscopic insight suggests that a flexible substructure consisting of corner-sharing polyhedra and distortion-relieving voids is beneficial to reduce volume change upon ion intercalation. For example, Wadsley-Roth and bronze phases with open tunnels (e.g., $Mo_3Nb_2O_{14}$) may exhibit small volume change upon H^+ intercalation while layered structures, such as α-MoO_3 and V_2O_5, undergo significant changes in the interlayer distances between their loosely stacked layers and a large volume change as a consequence.[6] On the other hand, perovskite family, which consist solely of corner-sharing octahedra, are not favorable as H^+-intercalation hosts owing to their low proton conductivities at room temperature;[13] the distance between oxide ions is too long for a proton to undergo anhydrous Grotthuss diffusion (consecutive H^+ rotation and hopping).[14] Note that near d^0 electron configurations of Mo and Nb contribute to the strain relief upon H^+ intercalation because their weakly directional M–O bonds allow for bending and twisting of O–M–O bridges, and site displacements of Mo/Nb[15] as indicated by structural analysis (Figure S16). In this context, other early transition metals (e.g., Ti^{4+}, V^{5+}, and W^{6+}) are likely to function as redox species with strain-relief effects when used in open-tunnel frameworks. Meanwhile, later transition metals (e.g., Fe^{3+}, Co^{3+}, and Ni^{3+}) may not be able to tolerate local

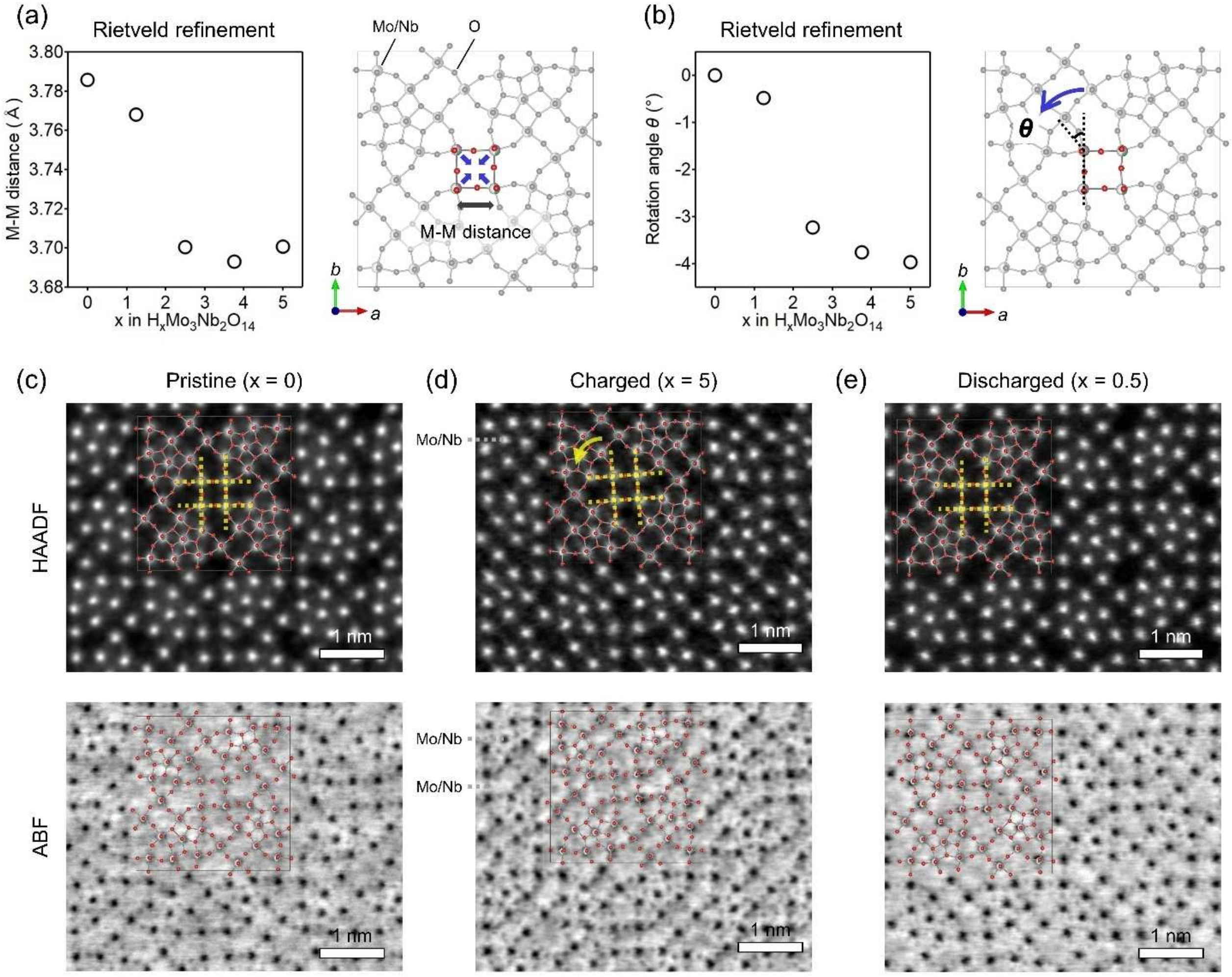

Figure 4. Mechanism for strain-free H^+ intercalation of $Mo_3Nb_2O_{14}$. Local structural changes calculated using the Rietveld-refined data for $H_xMo_3Nb_2O_{14}$. (a) M–M distance and (b) rotational angle of the square open tunnel at the center of the $Mo_3Nb_2O_{14}$ lattice viewed along the *c*-axis. HAADF- and ABF-STEM images of $H_xMo_3Nb_2O_{14}$ in its (c) pristine ($x=0$), (d) charged ($x=5$), and (e) discharged ($x=0.5$) states. The crystal structures shown in the STEM images were obtained by Rietveld refinement. Yellow-dotted lines highlight the rotation angles of the squares at the centers of the unit cells.

structural distortion upon H^+ intercalation because of their directional M–O bonds.[16]

Scanning transmission electron microscopy (STEM) is a powerful technique for visualizing the atomistic origin of the structural change (Figure S17). High-angle annular dark field (HAADF) images, where the image contrast is approximately proportional to the square of the atomic number ($\propto Z^2$), clearly show atomic columns of molybdenum and niobium, while annular bright-field (ABF) images ($\propto Z^{1/3}$) visualize atomic columns composed of light atoms, i.e., oxygen, in addition to those of molybdenum and niobium. The HAADF and ABF-STEM images of $Mo_3Nb_2O_{14}$ along the *c*-axis clearly show triangular, square, pentagonal, and hexagonal open tunnels (Figure 4c). The square open tunnel clearly rotates without any appreciable changes in atomic arrangement and lattice constants after H^+ intercalation (Figure 4d). Although the electron diffraction image of the charged sample shows forbidden reflections arising from broken symmetry (Figure S18), the volume change of Mo/NbO$_n$ ($n=6$ and 7) polyhedra in association with H^+ intercalation is cooperatively relieved by an open-tunnel buffer, reducing expansion of the *ab*-plane. The atomic arrangement completely recovers to that of the pristine state after H^+ deintercalation (Figure 4e).

Density functional theory (DFT) calculations were used to simulate the H^+ intercalation in $Mo_3Nb_2O_{14}$. Model structures of $H_xMo_3Nb_2O_{14}$ ($0 \leq x \leq 5$) with the most stable Mo/Nb site arrangement and H^+ distribution were prepared using a Coulombic and total energy-based screening approach, *EwaldSolidSolution* program to find optimal H^+ (forming O–H bond) configurations (Figure S19, see Methods section for further details).[17] All H^+ bond to oxide ions, but no specific oxide ions preferentially adsorbed H^+ (Figure S20). The $Mo_3Nb_2O_{14}$ lattice expands to give $\Delta V/V$ of 2.1 % at $x=5$ (Figure 5a), in stark contrast to $\Delta V/V$ upon Li^+ intercalation ($\Delta V/V = 5.5\,\%$). The smaller $\Delta V/V$ obtained for $H_xMo_3Nb_2O_{14}$ compared to that for $Li_xMo_3Nb_2O_{14}$ reproduces the experimental trend. The operating voltage for H^+ intercalation was calculated based on the total energy of $H_xMo_3Nb_2O_{14}$ and a chemical potential of hydrogen atom (Figure 5b and S21). H^+ intercalation occurs from 0.41 V for $x=0$ to -0.32 V vs. Ag/AgCl for $x=5$. Furthermore, density of state (DOS) calculations reveal that the empty electronic states of molybdenum (major contribution) and niobium (minor contribution) in $Mo_3Nb_2O_{14}$ shift below the Fermi level upon H^+ intercalation (Figure 5c and S22). Bader charge analysis also confirms decreases in the valence states of both Mo (major) and Nb (minor) (Figure S23).

DFT-based molecular dynamics (DFT-MD) simulations were conducted under *NVT* ensemble conditions to clarify the H^+-diffusion mechanism in $Mo_3Nb_2O_{14}$. The calculated trajectory clearly shows that H^+ rotates around Mo/NbO$_n$ ($n=6$ and 7) and hops three-dimensionally between oxide ions via the formation and cleavage of O–H bonds (Fig-

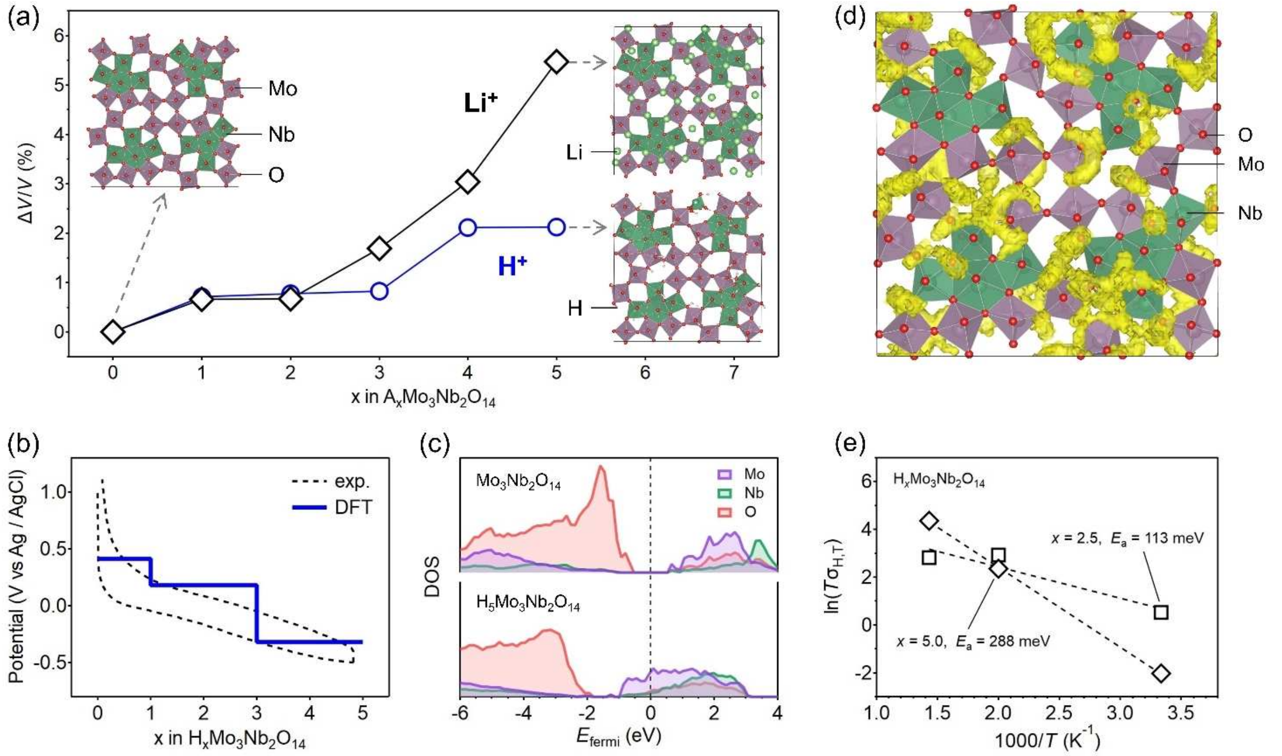

Figure 5. DFT calculations for H^+ intercalation into $Mo_3Nb_2O_{14}$. (a) Lattice volume change of $A_xMo_3Nb_2O_{14}$ (A = H, blue; A = Li, black). (b) Calculated operation potential of $Mo_3Nb_2O_{14}$ upon H^+ intercalation. The dashed line corresponds to the experimental charge/discharge curves for $Mo_3Nb_2O_{14}$ in 4.2 mol L^{-1} H_2SO_4/10H_2O–90PEG + 5 wt % HFE acquired during the second cycle. (c) Electronic densities of states of $H_xMo_3Nb_2O_{14}$ ($x=0$ and 5). (d) DFT-MD simulation with proton trajectory density for $H_{2.5}Mo_3Nb_2O_{14}$ at $T=700$ K and (e) the Arrhenius plots of proton conductivities for $H_xMo_3Nb_2O_{14}$ ($x=2.5$ and 5.0).

ure 5d). The mean-squared displacement (MSD) of H^+ was calculated at 300, 500, and 700 K for $H_{2.5}Mo_3Nb_2O_{14}$ (half-charged) and $H_5Mo_3Nb_2O_{14}$ (fully charged) (Figure S24); self-diffusion coefficients of 9.5×10^{-8} and 3.8×10^{-9} cm^2s^{-1} are calculated at 300 K for $H_{2.5}Mo_3Nb_2O_{14}$ and $H_5Mo_3Nb_2O_{14}$, respectively, while activation energies for H^+ diffusion are determined to be 113 and 288 meV, respectively (Figure 5e), which are comparable to those of α-MoO_3 and Brownmillerite $Sr_2Co_2O_5$.[18] These results indicate that $Mo_3Nb_2O_{14}$ may become capable of high power density after optimizing its particle size and improving ionic conductivity of electrolytes.

Finally, to demonstrate the concept of aqueous proton rechargeable batteries, we fabricated a full cell consisting of a $Mo_3Nb_2O_{14}$ anode and a vanadium hexacyanoferrate (VHCF, Figure S25) cathode,[19] and 4.2 $mol\,L^{-1}$ H_2SO_4/$10H_2O-90PEG$ ($x=90$) + 5 wt % HFE as the electrolyte (Figure 6a). The full cell delivers a specific capacity of 115 $mAh\,g^{-1}$ (per the weight of $Mo_3Nb_2O_{14}$) with an average voltage of 0.79 V at a specific current of 200 $mA\,g^{-1}$ (about 1 C for $Mo_3Nb_2O_{14}$) during early charge/discharge cycling (Figure 6b). The full cell retains 98.5 % of its initial specific capacity after 1000 cycles owing to the high electrochemical stability of the molecular crowding electrolyte and the structural integrity of $Mo_3Nb_2O_{14}$ (Figure 6c). The full cell exhibits a superior capacity retention compared to most rechargeable proton batteries reported in the literature (Table S2).

Conclusions

This study identifies H^+ intercalation with near-zero volume change in $Mo_3Nb_2O_{14}$, an open-tunnel bronze phase. A molecular crowding aqueous electrolyte (4.2 $mol\,L^{-1}$ H_2SO_4/$10H_2O-90PEG$ ($x=90$) + 5 wt % HFE) and a $Mo_3Nb_2O_{14}$ electrode synergistically establish a highly stable electrolyte-electrode system, providing a capacity retention of approximately 100 % and an average Coulombic efficiency of 99.99 % over 500 cycles. Detailed structural analyses reveal that the flexible open tunnel of $Mo_3Nb_2O_{14}$ undergoes rotation and shrinkage to relieve local structural change upon H^+ intercalation, resulting in near-zero volume change. Furthermore, $Mo_3Nb_2O_{14}$ shows solid-solution-type phase transition upon H^+ intercalation, which is also beneficial to reduce lattice mismatch. Owing to the strain-free properties, intraparticle cracking was suppressed after charge/discharge cycling. A full cell with the $Mo_3Nb_2O_{14}$ anode | 4.2 $mol\,L^{-1}$ H_2SO_4/$10H_2O-90PEG$ + 5 wt % HFE | VHCF cathode configuration operates stably with a capacity retention of 98.5 % after the 1000th cycle. This study not only highlights the importance of electrode materials with structural integrity for the development of aqueous proton batteries but also provides opportunities for the rational design of electrode materials that exhibit near-zero volume change.

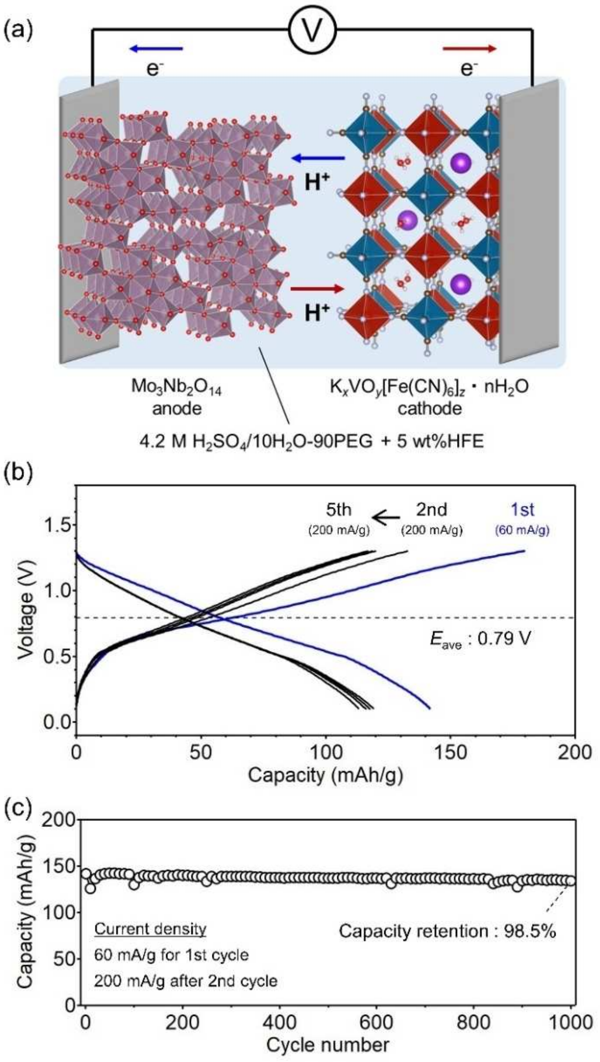

Figure 6. Electrochemical performance of a VHCF | $Mo_3Nb_2O_{14}$ full cell with 4.2 $mol\,L^{-1}$ H_2SO_4/$10H_2O-90PEG$ + 5 wt % HEF as the electrolyte. (a) Configuration of the full cell. (b) Galvanostatic charge/discharge curves for $Mo_3Nb_2O_{14}$ at a specific current of 200 $mA\,g^{-1}$ (about 1 C for $Mo_3Nb_2O_{14}$). (c) Cycle performance of $Mo_3Nb_2O_{14}$ at a specific current of 200 $mA\,g^{-1}$ (about 1 C for $Mo_3Nb_2O_{14}$). A low current density of 60 $mA\,g^{-1}$ (about 0.3 C for $Mo_3Nb_2O_{14}$) was applied for during the first cycle to activate cell performance. Note that specific capacities are calculated based on $Mo_3Nb_2O_{14}$.

Acknowledgements

This study was supported financially by the Core Research for Evolutional Science and Technology (CREST) Program (No. JPMJCR21O6) of JST, the Data Creation and Utilization Type Materials Research and Development Project (JPMXP1121467561) and Program for Promoting Research on the Supercomputer Fugaku (JPMXP1020200301 and JPMXP1020230325) of the Ministry of Education, Culture, Sports, Science, and Technology (MEXT), and the Kazuchika Okura Memorial Foundation. This work was supported by JSPS KAKENHI Grant-in-Aid for Transformative Research Areas (A) 'Ion Jamology' (Grant Number 24H02204). The authors are grateful to S.

Matsuoka of Waseda University for her support for the experiments. XPS and TEM were performed using research equipment (JPS-9010TR and JEM-2100: Material Characterization Central Laboratory) shared by the MEXT Project for Promoting Public Utilization of Advanced Research Infrastructure (Program for Supporting the Construction of Core Facilities) Grant Number JPMXS0440500023. TEM was performed at the Joint Research Center for Environmentally Conscious Technologies in Materials Science (Grant No. JPMXP0621467974) of ZAIKEN Waseda University. XRD and XAFS experiments were conducted at the BL5S2 and BL11S2 beamlines, respectively, of the Aichi Synchrotron Radiation Center, Aichi Science & Technology Foundation, Aichi, Japan (Proposal No.2022D4023 and 2023D3013). Specimen preparation for STEM observation was supported by Advanced Research Infrastructure for Materials and Nanotechnology (ARIM) of MEXT (Proposal No. JPMXP1223NM0152). STEM was performed at NIMS. The calculations were performed on the supercomputers at NIMS (Numerical Materials Simulator).

Conflict of Interest

The authors declare no conflict of interest.

Data Availability Statement

The data that support the findings of this study are available from the corresponding author upon reasonable request.

Keywords: aqueous battery · proton · bronze oxides · molecular crowding electrolyte

---

[1] F. Duffner, N. Kronemeyer, J. Tübke, J. Leker, M. Winter, R. Schmuch, *Nat. Energy* **2021**, *6*, 123–134.

[2] a) N. Bezginov, T. Valdez, M. Horbatsch, A. Marsman, A. C. Vutha, E. A. Hessels, *Science* **2019**, *365*, 1007–1012; b) W. Xiong, A. Gasparian, H. Gao, D. Dutta, M. Khandaker, N. Liyanage, E. Pasyuk, C. Peng, X. Bai, L. Ye, K. Gnanvo, C. Gu, M. Levillain, X. Yan, D. W. Higinbotham, M. Meziane, Z. Ye, K. Adhikari, B. Aljawrneh, H. Bhatt, D. Bhetuwal, J. Brock, V. Burkert, C. Carlin, A. Deur, D. Di, J. Dunne, P. Ekanayaka, L. El-Fassi, B. Emmich, L. Gan, O. Glamazdin, M. L. Kabir, A. Karki, C. Keith, S. Kowalski, V. Lagerquist, I. Larin, T. Liu, A. Liyanage, J. Maxwell, D. Meekins, S. J. Nazeer, V. Nelyubin, H. Nguyen, R. Pedroni, C. Perdrisat, J. Pierce, V. Punjabi, M. Shabestari, A. Shahinyan, R. Silwal, S. Stepanyan, A. Subedi, V. V. Tarasov, N. Ton, Y. Zhang, Z. W. Zhao, *Nature* **2019**, *575*, 147–150.

[3] L. Suo, O. Borodin, T. Gao, M. Olguin, J. Ho, X. Fan, C. Luo, C. Wang, K. Xu, *Science* **2015**, *350*, 938–943.

[4] Z. Su, J. Chen, W. Ren, H. Guo, C. Jia, S. Yin, J. Ho, C. Zhao, *Small* **2021**, *17*, 2102375.

[5] a) J. Xie, Z. Liang, Y.-C. Lu, *Nat. Mater.* **2020**, *19*, 1006–1011; b) S. Wu, J. Chen, Z. Su, H. Guo, T. Zhao, C. Jia, J. Stansby, J. Tang, A. Rawal, Y. Fang, J. Ho, C. Zhao, *Small* **2022**, *18*, 2202992; c) D. Kiburn, J. H. Roh, L. Guo, R. M. Briber, S. A. Woodson, *J. Am. Chem. Soc.* **2010**, *132*, 8690–8696; d) S. Nakano, D. Miyoshi, N. Sugimoto, *Chem. Rev.* **2014**, *114*, 2733–2758.

[6] Y. Lei, W. Zhao, J. Yin, Y. Ma, Z. Zhao, J. Yin, Y. Khan, M. N. Hedhili, L. Chen, O. Wang, Y. Yuan, X. Zhang, O. M. Bakr, O. F. Mohammed, H. N. Alshareef, *Nat. Commun.* **2023**, *14*, 5490.

[7] a) Y. Chen, D. Ma, K. Ouyang, M. Yang, S. Shen, Y. Wang, H. Mi, L. Sun, C. He, P. Zhang, *Nano-Micro Lett.* **2022**, *14*, 154; b) H. Jiang, J. J. Hong, W. Wu, T. W. Surta, Y. Qi, S. Dong, Z. Li, D. P. Leonard, J. J. Holoubek, J. C. Wong, J. J. Razink, X. Zhang, X. Ji, *J. Am. Chem. Soc.* **2018**, *140*, 11556–11559.

[8] P. Afanasiev, *J. Phys. Chem. B* **2005**, *109*, 18293–18300.

[9] a) J. Xie, Y. Guan, Y. Huang, Y.-C. Lu, *Chem. Mater.* **2022**, *34*, 5176–5183; b) D. E. Ciurduc, C. Cruz, N. Patil, A. Mavrandonakis, R. Marcilla, *Energy Storage Mater.* **2022**, *52*, 532–543.

[10] T. Shimizu, T. Nakai, K. Deguchi, K. Yamada, B. Yue, J. A. Ye, *Chem. Lett.* **2014**, *43*, 80–82.

[11] Y. Luo, E. Le Calvez, Y. Zhou, E. Gautron, E. Quarez, M. Preefer, O. Crosnier, J. N. Weker, L. Pilon, T. Brousse, B. Dunn, *Chem. Mater.* **2023**, *35*, 8675–8685.

[12] I. B. Bersuker, *Chem. Rev.* **2013**, *113*, 1351–1390.

[13] a) R. Haugsrud, T. Norby, *Nat. Mater.* **2006**, *5*, 193–196; b) T. Murakami, J. R. Hester, M. Yashima, *J. Am. Chem. Soc.* **2020**, *142*, 11653–11657; c) S. Fop, K. S. McCombie, E. J. Wildman, J. M. S. Skakle, J. T. S. Irvine, P. A. Connor, C. Savaniu, C. Ritter, A. C. Mclaughlin, *Nat. Mater.* **2020**, *19*, 752–757.

[14] W. Xu, K. Zhao, X. Liao, C. Sun, K. He, Y. Yuan, W. Ren, J. Li, T. Li, C. Yang, H. Cheng, Q. Sun, I. Manke, X. Lu, J. Lu, *J. Am. Chem. Soc.* **2022**, *144*, 17407–17415.

[15] a) D.-H. Seo, J. Lee, A. Urban, R. Malik, S. Kang, G. Ceder, *Nat. Chem.* **2016**, *8*, 692–697; b) N. Yabuuchi, M. Nakayama, M. Takeuchi, S. Komaba, Y. Hashimoto, T. Mukai, H. Shiiba, K. Sato, Y. Kobayashi, A. Nakao, M. Yonemura, K. Yamanaka, K. Mitsuhara, T. Ohta, *Nat. Commun.* **2016**, *7*, 13814; c) A. Urban, A. Abdellahi, S. Decek, N. Artrith, G. Ceder, *Phys. Rev. Lett.* **2017**, *119*, 176402.

[16] X. Zhao, Y. Tian, Z. Lun, Z. Cai, T. Chen, B. Ouyang, G. Ceder, *Joule* **2022**, *6*, 1654–1671.

[17] S.-H. Jang, R. Jalem, Y. Tateyama, *J. Phys. Chem. A* **2023**, *127*, 5734–5744.

[18] a) Z. Ma, X.-M. Shi, S. Nishimura, S. Ko, M. Okubo, A. Yamada, *Adv. Mater.* **2022**, *34*, 2203335; b) M. S. Islam, A. M. Nolan, S. Wang, Q. Bai, Y. Mo, *Chem. Mater.* **2020**, *32*, 5028–5035.

[19] X. Peng, H. Guo, W. Ren, Z. Su, C. Zhao, *Chem. Commun.* **2020**, *56*, 11803–11806.

Manuscript received: June 11, 2024
Accepted manuscript online: August 28, 2024
Version of record online: ■■, ■■

Forschungsartikel

Aqueous Proton Batteries

K. Kawai, S.-H. Jang, Y. Igarashi, K. Yazawa,
K. Gotoh, J. Kikkawa, A. Yamada,
Y. Tateyama, M. Okubo* ——— **e202410971**

Proton Intercalation into an Open-Tunnel Bronze Phase with Near-Zero Volume Change

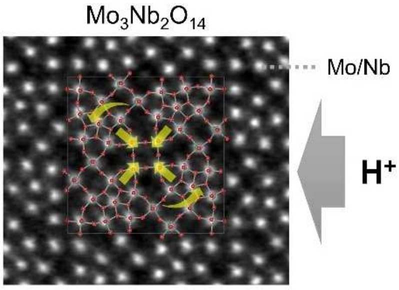

$Mo_3Nb_2O_{14}$ undergoes the near-zero volume change upon H^+ (de)intercalation in aqueous batteries owing to the open tunnels that buffer the local structure change of Mo/NbO_n polyhedra upon charge/discharge. The optimal molecular crowding electrolyte and the structural integrity of $Mo_3Nb_2O_{14}$ electrode synergistically establish a highly stable electrolyte-electrode system, providing a capacity retention of approximately 100 % over 500 cycles.